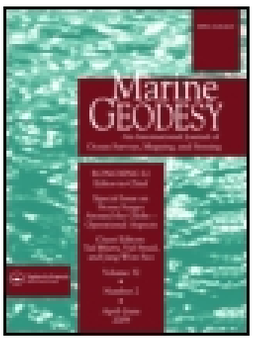

Marine Geodesy

ISSN: 0149-0419 (Print) 1521-060X (Online) Journal homepage: https://www.tandfonline.com/loi/umgd20

Acoustic Ray-Trace Equations for Seafloor Geodesy

C. David Chadwell & Aaron D. Sweeney

To cite this article: C. David Chadwell & Aaron D. Sweeney (2010) Acoustic Ray-Trace Equations for Seafloor Geodesy, Marine Geodesy, 33:2-3, 164-186, DOI: 10.1080/01490419.2010.492283

To link to this article: https://doi.org/10.1080/01490419.2010.492283

Marine Geodesy, 33:164–186, 2010

ISSN: 0149-0419 print / 1521-060X online
DOI: 10.1080/01490419.2010.492283

Taylor & Francis
Taylor & Francis Group

Acoustic Ray-Trace Equations for Seafloor Geodesy

C. DAVID CHADWELL AND AARON D. SWEENEY

Scripps Institution of Oceanography, University of California San Diego, La Jolla, California, USA

One goal of seafloor geodesy is to measure horizontal deformation of the seafloor with millimeter resolution. A common technique precisely times an acoustic signal propagating between two points to estimate distance and then repeats the measurement over time. The accuracy of the distance estimate depends upon the travel time resolution, sound speed uncertainty, and the degree to which the path computed from propagation equations replicates the actual path traveled by the signal. In this paper, we address the error from ray propagation equations by comparing three approximations to Snell's Law with ellipsoidal geometry.

Keywords GPS-acoustics, acoustic ranging, ellipsoid, deformation, plate motion

Introduction

Acoustics-based underwater geodesy measures horizontal displacements of the sea floor with millimeter resolution between points separated by a few meters to kilometers, spanning a single fault to an entire tectonic plate (e.g., Chadwell et al. 1999; Sweeney et al. 2005; Gagnon et al. 2005). The time-of-flight of an acoustic signal can be measured with ± 3 microsecond resolution (equivalent to 3 mm in range; Spiess et al. 1997). The propagation speed of the sound can be measured at the endpoints or preferably along the acoustic path by observing seawater temperature, conductivity (salinity), and pressure or with high frequency sound velocimeters (Sweeney et al. 2006). The travel time and sound speed can be combined to calculate a geometric distance underwater with centimeter or better resolution. In its simplest form, acoustic signals are transmitted from one seafloor unit to a second unit and back to the first to measure the two-way travel time. Typically, the two units are approximately one kilometer apart spanning a fault, and repeated interrogations over months to years measure the fault displacement, that is, deformation (Figure 1A). In deeper waters, where the units are below the turbulent influence of surface ocean processes, the sound speed increases with depth (pressure). Acoustic rays in this region are refracted upward and acoustic signals between units will tend to graze the sea floor. Towers are used to lift the ray endpoints above the sea floor, but as the horizontal separation increases beyond 2 km the tower height requirements grow to several meters and become impractical.

To avoid grazing the sea floor, one end of the ray path can be floated tens-of -meters up into the water column above the sea floor (Figure 1B). The distance between the seafloor

Received 18 September 2009; accepted 26 April 2010.
Address correspondence to C. David Chadwell, Marine Physical Lab, Scripps Institution of Oceanography, University of California San Diego, 9500 Gilman Drive, MS 0205, La Jolla, CA 92093-0205. E-mail: cchadwell@ucsd.edu

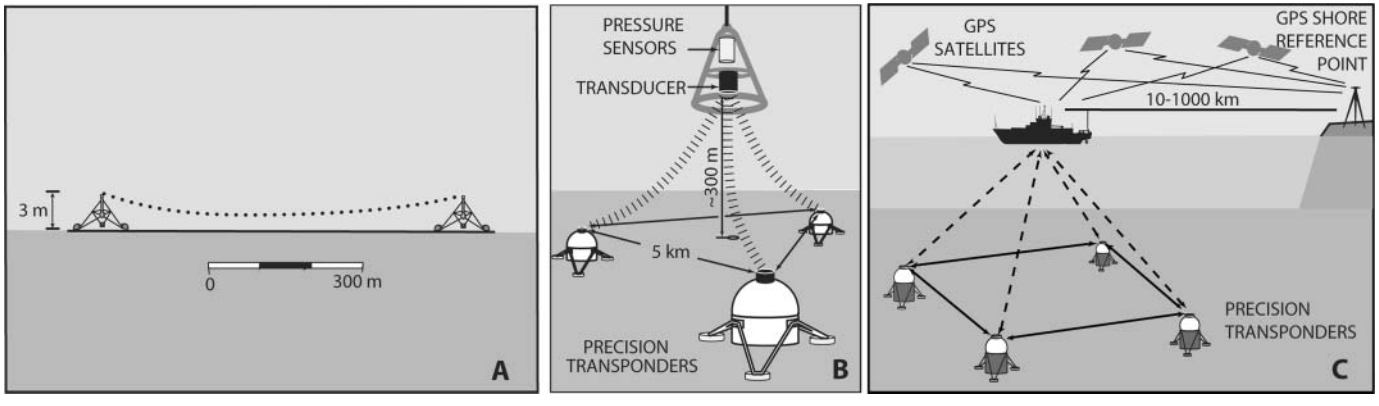

Figure 1. Direct path **(A)**, indirect path **(B)**, and GPS-acoustic **(C)** approaches to seafloor deformation measurements.

unit and the floating unit is, however, no longer a direct measure of deformation. Instead, at least two additional seafloor transponders are deployed, and a depth sensor is added to the floating unit. Two ranges and the depth, measured by tidally corrected pressure, uniquely triangulate the position of the floating unit (Sweeney et al. 2005). A range from a third seafloor unit will slightly over-determine the position of the floating unit. If the assumed relative positions of the three seafloor units are correct, the position triangulated for the floating unit from the three ranges will agree within the measurement uncertainty. If the assumed relative positions are incorrect, the disagreement among three ranges is proportional to corrections to the assumed seafloor unit locations. Multiple three-range fixes can be collected from throughout the array using several individual floating units dispersed around the array or by moving a vehicle around the array. The misfit from the various views across the array can be inverted to refine the relative positions of the seafloor units. Tracking the change in coordinates over time gives the deformation.

Sound speed uncertainty ultimately limits array sizes to a few kilometers before acoustic-derived distance uncertainty exceeds anticipated deformation signals ($\approx$ 1 cm). To span tectonic plates the floating unit is brought to the sea surface where its position is measured continuously with centimeter-level kinematic GPS (Figure 1C). The triangle or square defined by the seafloor units is tracked in the GPS frame from a ship or buoy held near the center of the seafloor array to minimize the impact of the predominately horizontally stratified sound speed. Three to five days of data are sufficient to determine the array's global position to less than a centimeter (Gagnon et al. 2005). Repeating the measurement campaigns through time gives the deformation.

While the acoustic-derived distance estimated between two towers is a direct measure of deformation, the distances from the seafloor unit to the floating unit or from the seafloor unit to the surface unit must be used indirectly. When employing either floating or surface units, a coordinate frame is adopted to relate distance measurements to coordinates of the seafloor units. To calculate the coordinates from the observed travel times, accurate mathematical models of the propagating acoustic ray must be constructed.

A global reference frame is needed to model the propagation of low frequency sound across ocean basins (Munk et al. 1988). In one experiment from 1960, sound was recorded after traveling halfway around the world (Shockley et al. 1982). More recently, the time of flight of sound traveling across ocean basins is used to detect small changes in the mean temperature of the ocean (Georges et al. 1986). Timing of modern signals is possible to $\pm$1 millisecond (range equivalent of $\sim$1 m). The propagation path follows generally the geodesic across the earth and is most easily and accurately described by ray propagation equations parameterized in ellipsoidal coordinates. These long range studies cover distances of about 10,000 km with timing resolution to $\pm$1 millisecond. Seafloor geodetic studies measure paths that are shorter by three orders of magnitude, 10 to 20 km, while simultaneously increasing the timing resolution by three orders of magnitude to $\pm$1 microsecond (range equivalent of $\sim$1 mm). Thus, calculations of distances with 1 mm resolution over 10–20 km also require ellipsoidal equations.

In this paper, we conduct a simulation to compare Snell's Law using ellipsoidal geometry with three approximations that use simpler geometries. The approximations are straight-ray (non Snell's Law) and Snell's Law with planar geometry, and Snell's Law with spherical geometry via an earth-flattening transformation. For the comparison, we choose a wide range of source and receiver depths and distances that are frequently encountered in acoustics-based seafloor geodesy.

Ellipsoidal Model

A rotational ellipsoid is one of the more accurate and practical analytical descriptions of the earth (Figure 2). The origin of the ellipsoid coincides with the center-of-mass of the earth and the ellipsoidal surface is defined by the semi-major (a) and semi-minor (b) axes. The separation between the ellipsoidal surface and the geoid, the geopotential surface of the earth that best approximates mean sea level, is the geoid undulation (N), which only varies between—107 m and +85 m across the entire globe (Lemoine et al. 1998). Positions are specified by latitude (ϕ), longitude (λ), and height (h) above the reference ellipsoid or as the orthometric height ($H = h - N$) above the geoid (Figure 3). Positions can also be specified in earth-centered earth-fixed (ECEF) coordinates:

$$\begin{aligned} X &= (N_\phi + h)\cos\phi\cos\lambda \\ Y &= (N_\phi + h)\cos\phi\sin\lambda \\ Z &= (N_\phi[1 - e^2] + h)\sin\phi, \end{aligned} \tag{1}$$

where N_ϕ, the radius of curvature in the prime vertical, is

$$N_\phi = \frac{a}{(1 - e^2\sin^2\phi)^{1/2}} \tag{2}$$

and e, the eccentricity, is

$$e^2 = \frac{a^2 - b^2}{a^2}. \tag{3}$$

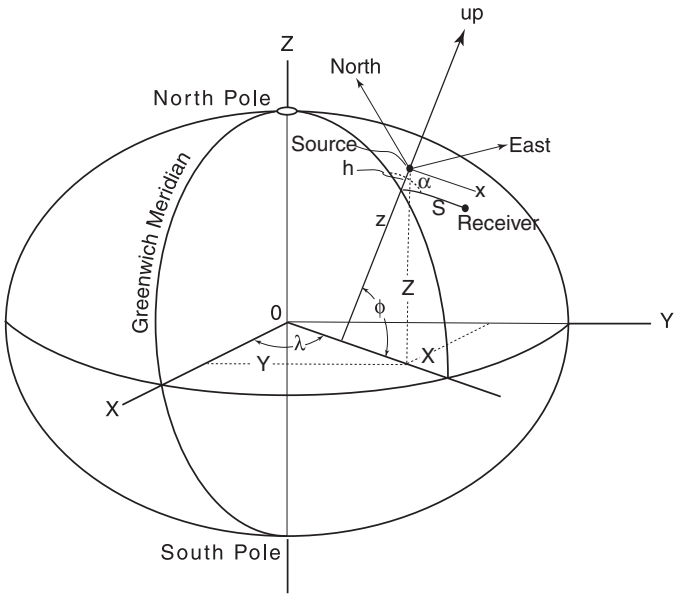

Figure 2. Ellipsoidal earth model with geodetic (ϕ, λ, h), earth-centered earth-fixed global (X,Y,Z), local horizon coordinates (e,n,u) and planar ray-trace frame (x,z).

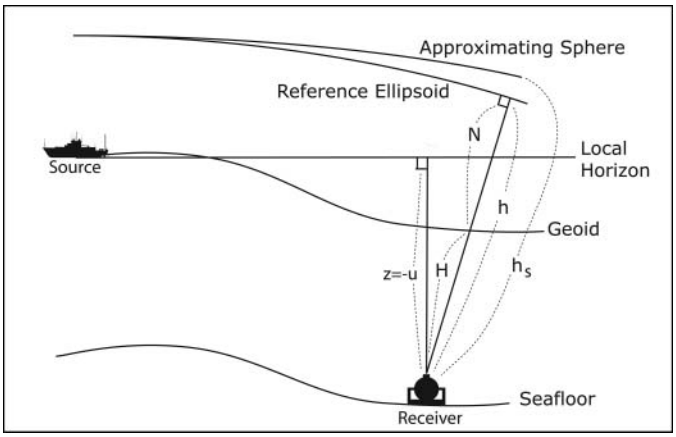

Figure 3. Expanded view of profile between source and receiver from Figure 2.

The meridional radius of curvature (M_λ) is

$$M_\lambda = \frac{a(1-e^2)}{(1-e^2\sin^2\phi)^{3/2}}. \tag{4}$$

The relationship between two points, for example, acoustic source and receiver, can be expressed by the shortest distance between the source and receiver points projected onto the ellipsoid, the geodesic (S), and the azimuth of the geodesic (α) from source to receiver, and their ellipsoidal heights. The relationship can also be expressed in local horizon coordinates (east, north, up) of the receiver relative to the source as

$$\begin{bmatrix} e_{rcv} \\ n_{rcv} \\ u_{rcv} \end{bmatrix} = \begin{bmatrix} -\sin\lambda_{src} & \cos\lambda_{src} & 0 \\ -\sin\phi_{src}\cos\lambda_{src} & -\sin\phi_{src}\sin\lambda_{src} & \cos\phi_{src} \\ \cos\phi_{src}\cos\lambda_{src} & \cos\phi_{src}\sin\lambda_{src} & \sin\phi_{src} \end{bmatrix} \begin{bmatrix} X_{rcv}-X_{src} \\ Y_{rcv}-Y_{src} \\ Z_{rcv}-Z_{src} \end{bmatrix}. \tag{5}$$

The acoustic frequencies used in this study (8 kHz to 17 kHz) are large compared to the sound speed gradient in depth making ray equations a suitable descriptor of acoustic propagation. Ray equations derived for an ellipsoidal earth describe the position along the ray specified by latitude, longitude, and ellipsoidal height (Yan 1999). The ray direction at any position (ϕ,λ) is specified by a ray angle (θ_e) downward from the local horizon and a ray azimuth (α_e) clockwise from North:

$$\frac{d\phi}{dh} = -\frac{\cos\alpha_e}{(M_\lambda + h)\tan\theta_e} \tag{6}$$

$$\frac{d\lambda}{dh} = -\frac{\sin\alpha_e}{(N_\phi + h)\ \cos\phi\ \tan\theta_e} \tag{7}$$

$$\frac{d\theta_e}{dh} = \cot\theta_e\left(\frac{\sin^2\alpha_e}{N_\phi + h} + \frac{\cos^2\alpha_e}{M_\lambda + h}\right) - \frac{1}{c(\phi,\lambda,h)}\left[\frac{\cos\alpha_e}{M_\lambda + h}\frac{\partial c}{\partial\phi} + \frac{\sin\alpha_e}{(N_\phi + h)\cos\phi}\frac{\partial c}{\partial\lambda} + \cot\theta_e\frac{\partial c}{\partial h}\right] \tag{8}$$

$$\frac{\mathrm{d}\alpha_\mathrm{e}}{\mathrm{d}h} = -\frac{\tan\phi\sin\alpha_\mathrm{e}}{(N_\phi + h)\tan\theta_\mathrm{e}} - \sin\alpha_\mathrm{e}\,\cos\alpha_\mathrm{e}\left(\frac{1}{N_\phi + h} - \frac{1}{M_\lambda + h}\right) + \frac{1}{\sin\theta_\mathrm{e}\cos\theta_\mathrm{e}}\frac{1}{c(\phi,\lambda,h)}\left[-\frac{\sin\alpha_\mathrm{e}}{(M_\lambda + h)}\frac{\partial c}{\partial\phi} + \frac{\cos\alpha_\mathrm{e}}{(\mathrm{N}_\phi + h)\cos\phi}\frac{\partial c}{\partial\lambda}\right] \tag{9}$$

and propagation time (t) as

$$\frac{\mathrm{d}t}{\mathrm{d}h} = -\frac{1}{c\,(\phi,\lambda,h)\ \sin\theta_\mathrm{e}} \tag{10}$$

where $c\,(\phi, \lambda, h)$ is sound speed defined in the following section.

Sound Speed

Solutions to Eqs. (8)–(10) require knowledge of the sound speed ($c\,(\phi, \lambda, h, t)$), which varies in both space and time in the ocean. Variability significant to seafloor geodetic ranging can occur over regions of hundreds of kilometers driven by mesoscale oceanographic processes lasting from weeks to months or longer. It can also occur over regions of hundreds of meters driven by internal waves and tides lasting from approximately 20 minutes to tidal periods.

Regional changes are too wide and gradual to be detectable as lateral variations over the few kilometer span of a seafloor geodesy array. However, their cumulative effect over time can change the mean vertical structure of the sound speed field. In actual experiments, an attempt is made to measure the sound speed by continuously profiling a conductivity (salinity), temperature, and depth (pressure) measuring device from the sea surface to the sea floor for three to five days. The CTD measurements are used to calculated the sound speed and capture any changes in the vertical structure of the sound speed due to broader oceanographic processes, coincident with seafloor geodetic ranging. For experiments that are conducted as annual campaigns repeated over several years, this approach effectively removes long-term changes in sound speed.

Local effects are dominated by internal waves of ~20 minute periods with lateral extent of several hundred meters or more and vertical extent from the surface to a depth of a few hundred meters. The spatial wavelength of the internal wave means that at any instant at a fixed ellipsoidal height ($c(\phi, \lambda, h = \text{constant})$), sound speed can vary laterally a few parts in 10^4 to 10^5 over a kilometer-wide span of the acoustic path. This is significant but difficult to measure in the real ocean. This effect can be minimized in GPS-acoustic data by averaging over 3–5 days, which are many temporal cycles of the internal waves passing laterally through the array (e.g., Spiess et al. 1998). It is avoided in most direct and indirect path data by operating near the seafloor in deep water well below the mixed layer and in a region of lateral homogeneity (Sweeney et al. 2005). Finally, no temporal or spatial variability significant to seafloor geodetic ranging occurs over the few second span of a single propagating ray. Therefore, all temporal and spatial variability of sound speed that is driven by oceanographic process and is significant to seafloor geodesy has been accommodated by the above described operational and data collection practices. This reduces sound speed dependence to the form of $c\,(h)$ for the numerical analysis performed in this paper.

Next, we address one nonoceanographic source of lateral variations. The conversion of the vertical reference for sound speed profiles from relative to mean sea level to ellipsoidal surface requires the geoid undulation (N) which varies with location. In CTD profiles the

vertical reference for the pressure (depth) measurements is the mean sea surface. With mean sea level approximated by the geoid, orthometric height (H), which is negative downward from the geoid, is the same magnitude, but opposite sign of depth (d), the more common oceanographic vertical coordinate that is positive downward from mean sea level (i.e., $d = -H$). Orthometric height is related to ellipsoidal height (h) as $h = H + N$, where N is the geoid undulation and a function of position (ϕ and λ), giving $h = -d + N$. With the introduction of the geoid undulation, sound speed again becomes a function of geodetic position $c(h) = c(H + N(\phi, \lambda)) = c(-d + N(\phi, \lambda))$. For example, at a seafloor trench the GPS/acoustic arrays off the coast of Peru span a region where the geoid undulation changes by as much as 41 cm from east to west over 5 km (Gagnon et al. 2005). However, in determining the sound speed via a CTD profile, the depths in the profile are typically accurate to only 1 m. We therefore neglect the range-dependency introduced by changes in the geoid undulation from acoustic source to receiver and adopt a mean value $\bar{N}$ for the array. Thus, once again sound speed is reduced to a function of ellipsoid height in the equations for ray angle (Eq. (8)) and ray azimuth (Eq. (9)), which amounts to neglecting the sound speed derivatives as a function of latitude and longitude, and in the equation for propagation time (Eq. (10)).

Sound speed varies greatly (few parts in 10^2) in the vertical and for the purposes of this study can be modeled in canonical form as:

$$c(d_F) = c_o \left[1 + \varepsilon(\eta + \exp^{-\eta} - 1)\right] \tag{11}$$

with the dimensionless distance beneath the depth of the sound channel axis as

$$\eta = \frac{2(d_F - D)}{B} \tag{12}$$

where the sound channel axis depth is $D = 1300$ m, the sound velocity at this depth is $c_o = 1492$ m/s, $B = 1300$ m is the stratification scale, and $\varepsilon = 7.4 \times 10^{-3}$ is the perturbation coefficient (after Munk 1974; Figure 4). Here d_F is the depth from the mean sea level realization in each coordinate frame denoted by subscript F. In the case of the ellipsoid frame ($F = e$) and $d_e = -h + \bar{N}$. In subsequent discussions of the local horizon frame ($F = p$) and $d_p = -u$ where u is the up coordinate in the local horizon frame. Finally, in the planar ray-trace frame ($F = r$) and depth is $d_r = z$.

In practice, to reduce computation time, the sound speed profiles calculated from in-situ CTD measurements or sound velocimeters are approximated for ray-tracing calculations as layers ~1 m thick near the surface increasing to 5–10 m at greater depth. To simulate layering with the theoretical profile generated from Eqs. (11) and (12), the continuous profile is approximated as stacked horizontal layers of constant gradient (b)

$$c(d_F) = c(\langle d_F \rangle_i) + b_i(d_F - \langle d_F \rangle_i) \tag{13}$$

where $\langle d_F \rangle_i \leq d_F \leq \langle d_F \rangle_{i+1}$ and $\langle d_F \rangle_i$ and $\langle d_F \rangle_{i+1}$are the upper and lower bounds of the layer, respectively and $b_i = \frac{c(\langle d_F \rangle_{i+1}) - c(\langle d_F \rangle_i)}{\langle d_F \rangle_{i+1} - \langle d_F \rangle_i}$. Here, d_F is the depth defined by the coordinate frame under consideration (e.g., $d_e = -h + \bar{N}$ in the global frame or $d_p = -u$ in the local horizon frame or $d_r = z$ in the planar ray-trace frame).

Numerical Simulations

The ray equations for the ellipsoidal model of the earth are adopted as accurate descriptions of a propagating ray in the real ocean. The source lies at the sea surface and the receiver at

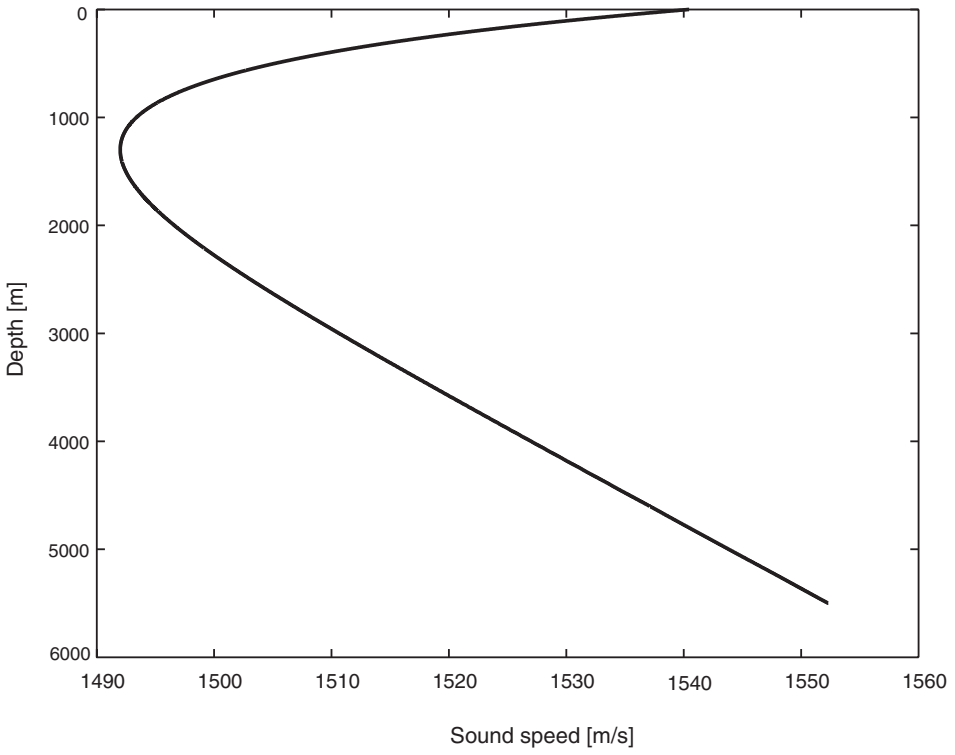

Figure 4. Canonical sound speed profile after Munk (1974).

the sea floor and travel times are calculated for several combinations of the receiver depth, the distance on the ellipsoid, the latitude, and the azimuth between source and receiver. Acoustic-based seafloor geodetic systems operate in seafloor water depths from 100 to > 5000 m. As a representative sample, simulations are computed for water depths of 100, 500, 1000, 2500, and 5000 m. Ray lengths are limited in shallower waters by refraction and reflection and in deep water by sound speed uncertainty. A representative span of ranges is generated by multiplying each sample water depth by 1, 2, 3, and 4. For example, at a depth of 500 m the ranges are 500, 1000, 1500, and 2000 m; at 5000 m depth ranges are 5000, 10000, 15,000, and 20,000 m. Ray dependence on latitude and azimuth is examined by repeating the depth and range values with source points at latitudes of 0°, 30°, and 45° with azimuths of 0°, 45°, and 90° to the receiver. Because the ellipsoid is rotationally symmetric, the computations are independent of longitude.

For each of the permutations, the receiver position is calculated from the source position given the source latitude and distance and azimuth to the receiver (Vincenty 1975). Starting with the geodetic vertical angle and azimuth as an initial guess for the ray angle and azimuth, ellipsoidal ray equations (Eqs. (6)–(9)) are integrated with a fourth-order Runga-Kutta approach with adaptive stepwise control to arrive at the receiver location. The initial ray angle and azimuth are adjusted using the downhill simplex method until the propagated ray arrives within 0.05 mm of the known receiver position. Once the ray angle and azimuth are known, the travel time (t_e) is computed along this ray by integrating Eq. (10). In the following, approximations to the ellipsoidal solutions are examined and compared with t_e which allows determination of the accuracy of each approximation.

Straight-Ray with Planar Approximation

A widely used straight-ray approximation uses Eq. (5) to transform the receiver point into a local horizon system at the source point and calculates the geometric range between the two points and divides by an average sound speed to calculate the average travel time

$$t_a = \frac{\sqrt{e_{rcv}^2 + n_{rcv}^2 + u_{rcv}^2}}{c_m} \tag{14}$$

where e_{rcv} and $n_{rcv}$are the receiver east and north coordinates respectively, and the mean sound speed (c_m) between the source depth ($-u_{src}$) and the receiver depth ($-u_{rcv}$) is defined as:

$$c_m = \frac{-u_{src} - (-u_{rcv})}{\int_{-u_{rcv}}^{-u_{src}} \frac{du}{c(u)}} \tag{15}$$

The travel time $t_a$is computed for each source/receiver pair in the permutation set used to compute the travel time t_e from the ellipsoidal ray equations. The time difference, $|t_a - t_e|$, is multiplied by a nominal sound speed of 1500 m/s to convert the time difference into distance which is then resolved into horizontal and vertical components as plotted in Figure 5. At 5 km depth, the error in the horizontal component of the ray is 10 cm at 5 km range, but exceeds 10 m at 20 km range. In fact, only the 100 m range at 100 m depth is below the 1 mm error threshold (dashed horizontal line in Figure 5). A similar pattern is observed in the vertical component of the range error (Figure 5B). The straight-ray approximation is not sufficient for millimeter-level seafloor deformation except over short (<100 m) distances.

Snell's Law with Planar Approximation

The next enhancement dispenses with the straight ray description and adopts Snell's Law to describe the ray propagation as

$$k = \frac{\cos\theta}{c} \tag{16}$$

where k is the ray parameter or constant, θ is the angle of the ray with respect to the horizontal, and c is the sound speed. A nominal ray propagating under Snell's Law in a velocity increasing with depth is shown in Figure 6 in the planar ray-trace frame x,z. The relationship between the x,z coordinates of the planar ray-trace frame and the e,n,u local horizon coordinates is $x = \sqrt{e^2 + n^2}$ and $z = -u$.

From Figure 6, the differentials

$$ds = cdt \tag{17}$$

$$\frac{dz}{ds} = \sin\theta \tag{18}$$

and

$$\frac{dx}{dz} = \cot\theta \tag{19}$$

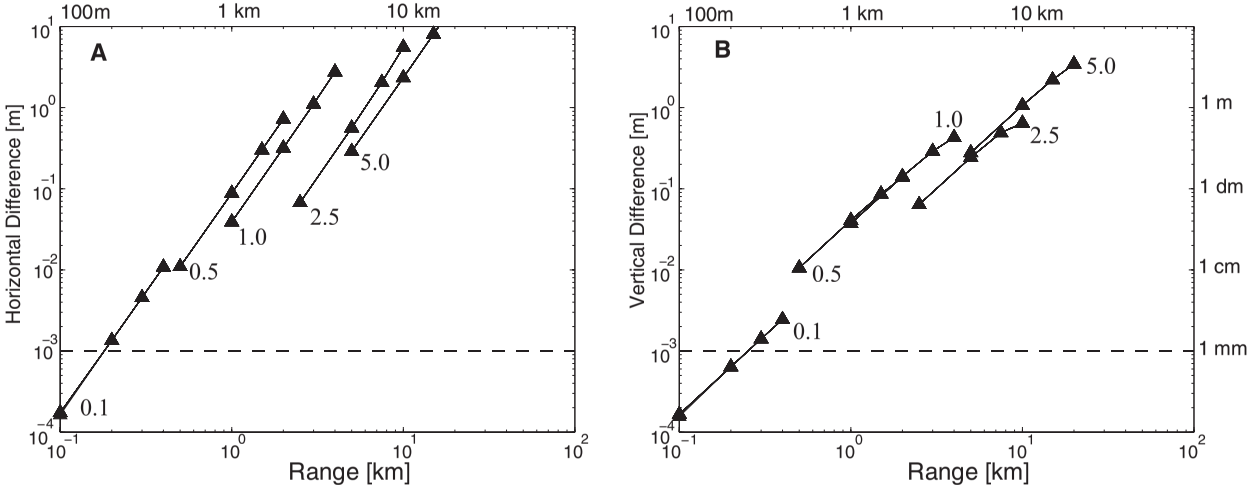

Figure 5. Horizontal (**A**) and vertical (**B**) difference between the straight-ray and ellipsoidal models compared over depths of 0.1, 0.5, 1.0, 2.5, and 5.0 km with ranges of 1, 2, 3, and 4 times the depth. Each curve is a different receiver depth (labeled) at four range values. Dashed horizontal line is the 1 mm threshold.

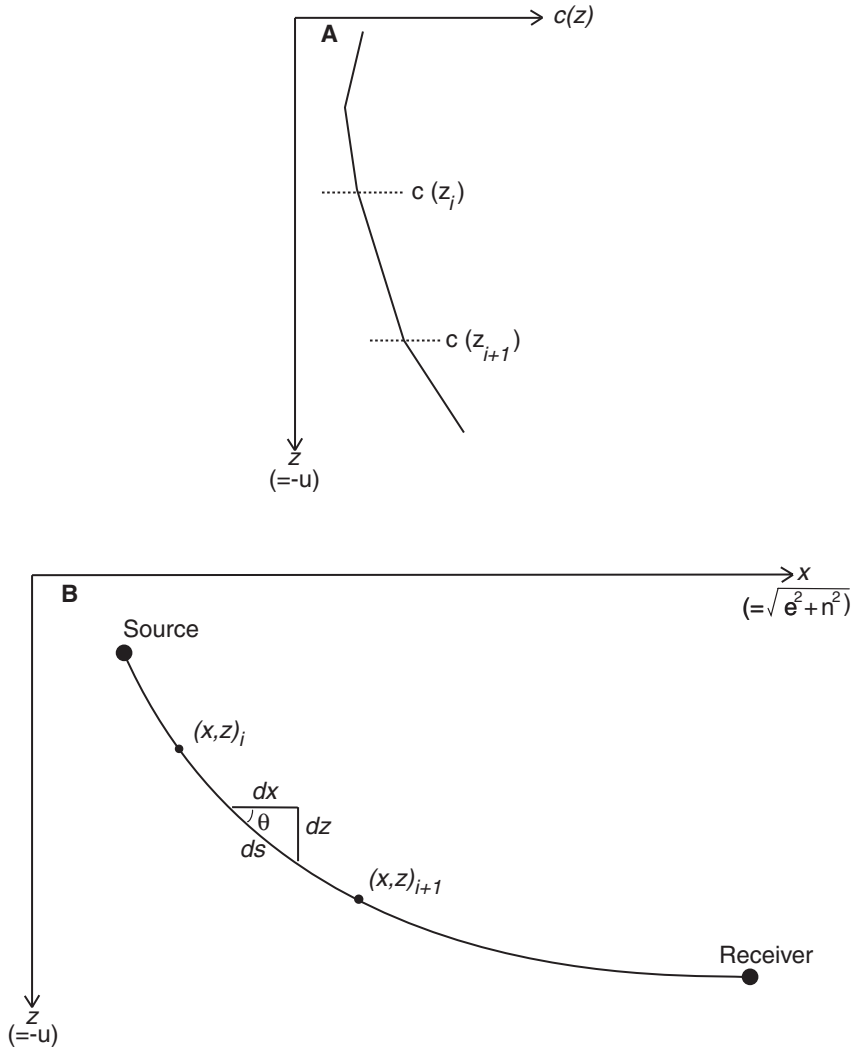

Figure 6. (**A**) Layered sound speed profile and (**B**) the nominal ray propagation following Snell's Law in a sound speed increasing linearly with depth ($d_r = z$) in a 2-D planar ray-trace coordinate geometry (x,z).

are formed by inspection. From Eqs. (17) and (18) the travel time is

$$dt = \frac{ds}{c}$$

$$t_{i+1} - t_i = \int_{z_i}^{z_{i+1}} \frac{ds}{c} = \int_{z_i}^{z_{i+1}} \frac{dz}{c \sin\theta}. \tag{20}$$

From Eq. (19) the horizontal distance is

$$x_{i+1} - x_i = \int_{z_i}^{z_{i+1}} \cot\theta dz \tag{21}$$

From Snell's Law the following trigonometric expressions can be formed as

$$\sin\theta = \sqrt{1 - k^2c^2} \tag{22}$$

$$\cot\theta = \frac{kc}{\sqrt{1 - k^2c^2}} \tag{23}$$

Substituting Eqs. (22) and (23) into Eqs. (20) and (21), respectively, gives

$$t_{i+1} - t_i = \int_{z_i}^{z_{i+1}} \frac{dz}{c\sqrt{1 - k^2c^2}} \tag{24}$$

$$x_{i+1} - x_i = \int_{z_i}^{z_{i+1}} \frac{kcdz}{\sqrt{1 - k^2c^2}} \tag{25}$$

The variation of sound speed with depth is approximated to a high degree as a stack of layers. Within each layer the sound speed has a constant gradient as given in Eq. (13), which in the planar ray-trace frame with $d_r = z$ becomes

$$c(z) = c(z_i) + b_i(z - z_i) \tag{26}$$

where $z_i \leq z \leq z_{i+1}$ and z_i and z_{i+1} are the upper and lower bounds of the layer, respectively. To solve Eqs. (24) and (25) the following substitution of variables is defined

$$w \equiv \frac{c(z_i)}{b_i} + (z - z_i) \tag{27}$$

$$dw = dz \tag{28}$$

$$c(w) = b_i w \tag{29}$$

Eqs. (24) and (25) become

$$t_{i+1} - t_i = \int_{w_i}^{w_{i+1}} \frac{dw}{b_i w\sqrt{1 - k^2b_i^2w^2}} \tag{30}$$

$$x_{i+1} - x_i = \int_{w_i}^{w_{i+1}} \frac{kb_i w\, dw}{\sqrt{1 - k^2b_i^2w^2}} \tag{31}$$

The closed form solution can be found from integral tables as

$$x_{i+1} - x_i = \frac{1}{kb_i}\left[-\left(1 - k^2b_i^2w_{i+1}^2\right)^{\frac{1}{2}} + \left(1 - k^2b_i^2w_i^2\right)^{\frac{1}{2}}\right] \tag{32}$$

$$t_{i+1} - t_i = \frac{1}{b_i}\ln\left[\frac{w_{i+1}\left[1 + \left(1 - k^2b_i^2w_{i+1}^2\right)^{\frac{1}{2}}\right]}{w_i\left[1 + \left(1 - k^2b_i^2w_i^2\right)^{\frac{1}{2}}\right]}\right] \tag{33}$$

The total distance and travel time are the summations of Eqs. (32) and (33) from the source depth (z_{src}) to receiver depth (z_{rcv}) given by

$$x_{src-rcv} = \sum_{z_{src}}^{z_{rcv}} (x_{i+1} - x_i) \tag{34}$$

and

$$t_p = t_{src-rcv} = \sum_{z_{src}}^{z_{rcv}} (t_{i+1} - t_i) \tag{35}$$

Each depth and range combination in the permutation set defines a total length S on the ellipsoid between the source and receiver. Beginning with an approximation to the ray angle from $\sin\theta = \frac{u_{rcv}}{\sqrt{e_{rcv}^2+n_{rcv}^2+u_{rcv}^2}}$, the ray angle is adjusted until the sum $x_{src-rcv}$ in Eq. (34) formed from Eq. (32) applied across each sound speed layer from the source to the receiver matches the geodesic$S$. This ray angle is held fixed and Eq. (33) applied from source to receiver summing (Eq. (35)) to t_p the travel time for Snell's Law with a planar model. The travel time (t_p) is computed for each source/receiver pair used to compute the travel time (t_e) from the ellipsoidal ray equations. The difference, $\left|t_p - t_e\right| \times 1500$ m/s, is calculated and resolved into horizontal and vertical components plotted in Figure 7. The useful range over which the planar equations can be used is extended up to 1 km in 100 and 500 m water depths as compared to the straight-ray, an improvement but still unsuitable for deep water applications.

Snell's Law with Spherical Approximation

The next enhancement is to move from a planar frame to a spherical frame. The earth can be approximated as a sphere whose center coincides with the origin of the reference ellipsoid. In spherical coordinates, the position of any point is given by a spherical latitude, Φ (positive north of the sphere's equator), a spherical longitude, Λ (positive east of the sphere's reference meridian), and a spherical height, h_s (positive upward from the reference sphere in the radial direction).

The ray equations become:

$$\frac{\mathrm{d}\Phi}{\mathrm{d}h_\mathrm{s}} = -\frac{\cos\alpha_\mathrm{S}}{(R+h_\mathrm{s})\ \tan\theta_\mathrm{S}} \tag{36}$$

$$\frac{\mathrm{d}\Lambda}{\mathrm{d}h_\mathrm{s}} = -\frac{\sin\alpha_\mathrm{S}}{(R+h_\mathrm{s})\ \cos\Phi\ \tan\theta_\mathrm{S}} \tag{37}$$

$$\frac{\mathrm{d}\theta_\mathrm{S}}{\mathrm{d}h_\mathrm{s}} = -\cot\theta_\mathrm{S}\left(\frac{1}{c(h_\mathrm{s})}\frac{dc}{dh_s} - \frac{1}{R+h_\mathrm{s}}\right) \tag{38}$$

$$\frac{\mathrm{d}\alpha_\mathrm{S}}{\mathrm{d}h_\mathrm{s}} = -\frac{\tan\Phi\ \sin\alpha_\mathrm{S}}{(R+h_\mathrm{s})\tan\theta_\mathrm{S}} \tag{39}$$

where θ_s is the ray angle downward from the local horizon, α_s is the ray azimuth clockwise from North, and R is the radius of the sphere.

A globally best-fitting ellipsoid with origin coinciding with the earth's center-of-mass was selected as the best practical approximation to the earth. It is reasonable to propose a global sphere centered at the earth's center-of-mass as the best spherical approximation. One likely candidate is the mean of the semi axes of the ellipsoidal earth,R_M, is

$$R_\mathrm{M} = \frac{2a+b}{3} \tag{40}$$

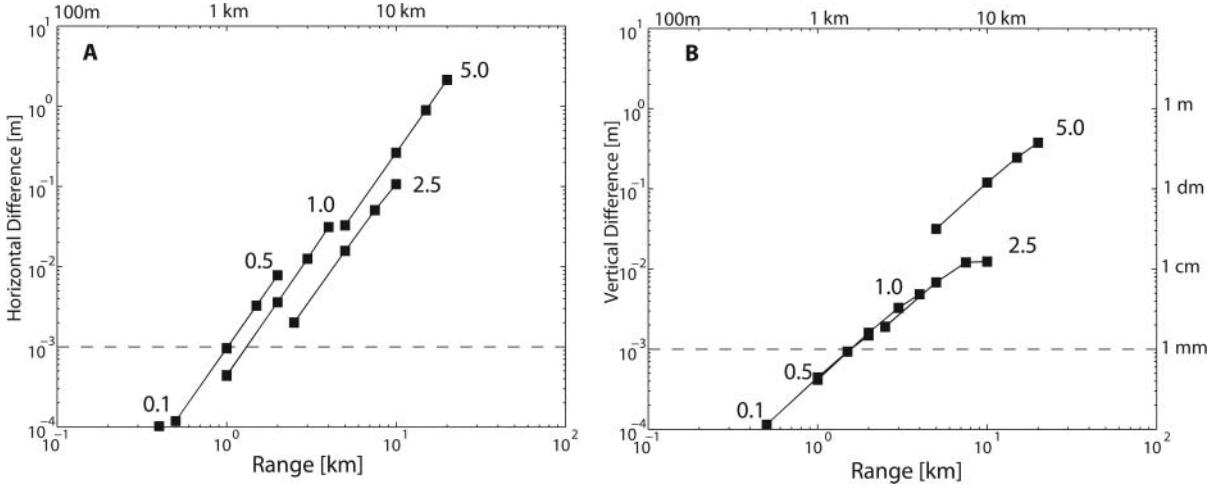

Figure 7. Horizontal (**A**) and vertical (**B**) difference between the Snell's Law ray with planar geometry and ellipsoidal model compared over depths of 0.1, 0.5, 1.0, 2.5, and 5.0 km with ranges of 1, 2, 3, and 4 times the depth. Each curve is a different receiver depth (labeled) at four range values. Dashed horizontal line is the 1 mm threshold.

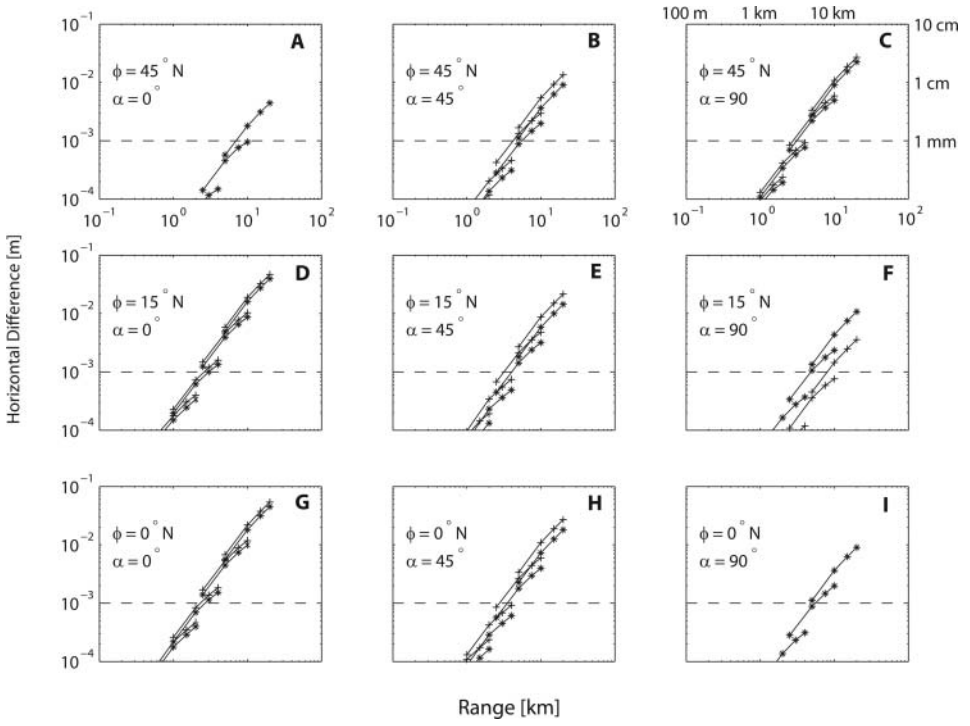

Figure 8. Horizontal difference between Snell's Law planar form with earth flattening transformation applied using global mean radius R_M (asterisks) and distance from earth center R_R (pluses) and the ellipsoid model. Note that the maximum vertical scale is reduced to 10 cm compared to 10 m in Figures 5 and 7. Separate plots show dependence on source latitude and ray azimuth.

where a is the radius of the earth in the equatorial plane (semi-major axis of the ellipse) and b is the radius of the earth in any meriodonal plane (semi-minor axis of the ellipse). Another alternative is to compute the radius at a point from the earth's center, R_R, as

$$R_R = \sqrt{X^2 + Y^2 + Z^2} \tag{41}$$

where (X,Y,Z) are the earth-centered earth-fixed coordinates of the source point. Each different source location requires a new radius R_R and defines a new sphere for calculations.

The spherical approximations centered at the earth's center decrease the difference with the ellipsoidal model from approximately 2 m for the rectangular case to approximately 3 cm (Figures 8 and 9). However, the maximum range is still limited to approximately 2 km to remain below the 1 mm threshold. Generally, neither R_R nor R_M provide a good fit to the local ellipsoidal surface because the spheres they define are not generally tangent to the ellipsoid at the point of interest. The key is to have the approximating sphere tangent to the ellipsoid in the region of interest. This is best accomplished by choosing the radius of the sphere to be a combination of the local ellipsoid radii of curvature in the prime vertical N_ϕ and the meridian M_λ.

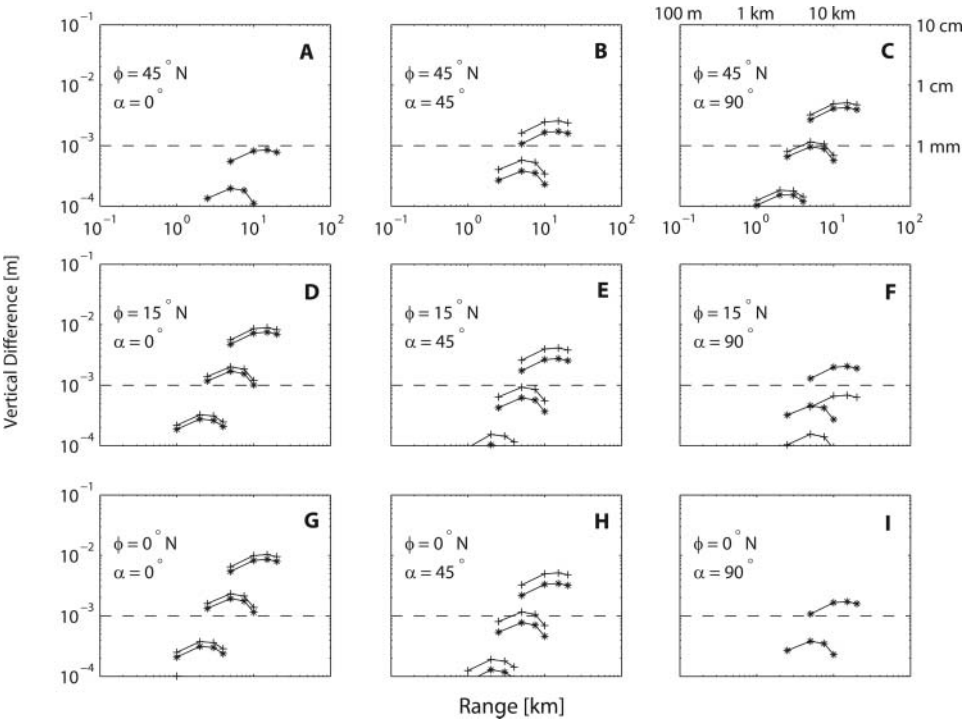

Figure 9. Vertical difference between Snell's Law planar form with earth flattening transformation applied using global mean radius R_M (asterisks) and distance from earth center R_R (pluses) and the ellipsoid model. Note that the maximum vertical scale is reduced to 10 cm compared to 10 m in Figures 5 and 7. Separate plots show dependence on source latitude and ray azimuth.

The problem with the implementation of these locally tangent spheres is that their origins are no longer at the origin of the rotational ellipsoid and the ECEF Cartesian system. The translation between the origins of the tangential sphere and the rotational ellipsoid must be determined for each new point. This is tractable but cumbersome to implement. An alternative approach is to project the endpoints and sound speed profile from the spherical earth to a rectangular earth via a so-called "flat earth transformation" (Biswas and Knoppoff 1970). The "flattened" heights (h_f) are related to the original ellipsoidal heights (h) by

$$h_f = R \ln\left(\frac{R}{R-h}\right) \tag{42}$$

and the "flattened" sound speed profile is related to the original profile by

$$c_f(h_f) = c(h)\frac{R}{R-h} \tag{43}$$

where R is a radius of the earth. These transformed values can be integrated with the rectangular equations for which the closed form was given in Eqs. (32)–(35) while accommodating the earth's spherical surface. The definition of the radius R that best approximates locally the ellipsoid is all that remains to implement the equations.

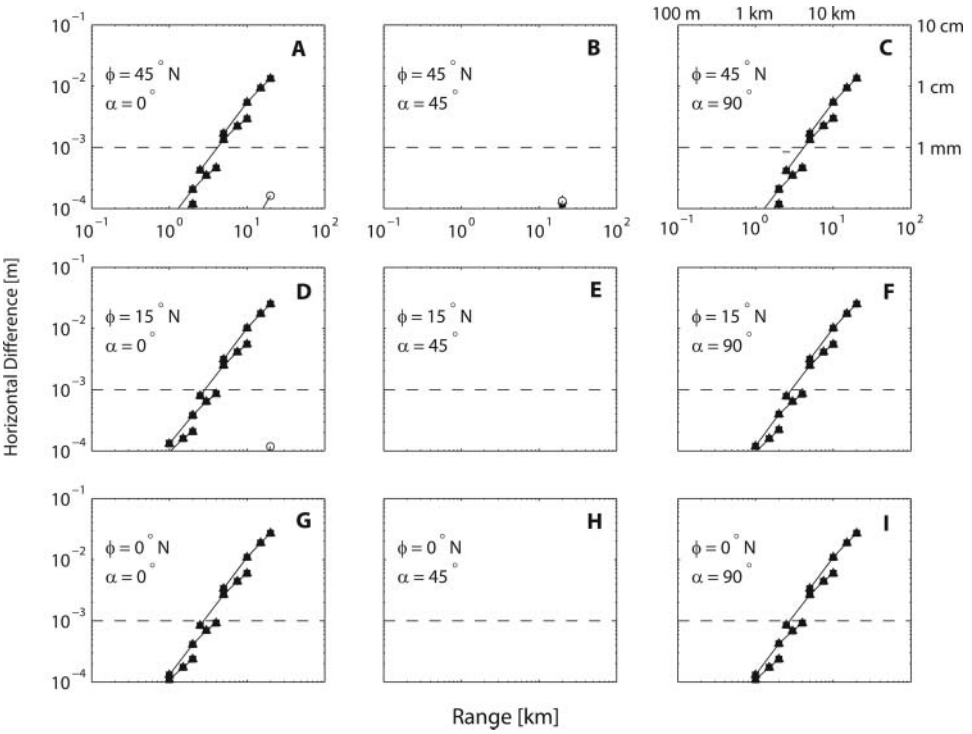

Figure 10. Horizontal difference between Snell's Law planar form with earth flattening transformation applied using local mean radius, R_{L}(triangles), Gaussian mean radius, R_{G} (squares), and radius along the azimuth, R_α (circles) and the ellipsoid model. Note that the maximum vertical scale is reduced to 10 cm compared to 10 m in Figures 5 and 7. Separate plots show dependence on source latitude and ray azimuth. In all cases, choosing the radius along the azimuth, R_α, results in submillimeter agreement with the ellipsoidal earth ray-trace model.

The radius of curvature in the prime vertical (N_ϕ) and meridian (M_λ) are both tangent to the ellipsoid at the given point in their respective planes, but not in a general direction. Here, a combination of the two radii is used to define a nominally tangent local sphere. There are several standard combinations of these radii. The local mean radius, R_{L}, or more precisely, the inverse of the mean curvature, is

$$R_{\mathrm{L}} = \frac{1}{\frac{1}{2}\left(\frac{1}{M_\lambda} + \frac{1}{N_\phi}\right)} \tag{44}$$

The Gaussian mean radius of curvature is

$$R_G = \sqrt{M_\lambda N_\phi} \tag{45}$$

These two are essentially averages over all azimuths at the point. The radius along the azimuth (α) from source to receiver, R_α, is

$$R_\alpha = \frac{1}{\frac{\cos^2\alpha}{M_\lambda} + \frac{\sin^2\alpha}{N_\phi}} \tag{46}$$

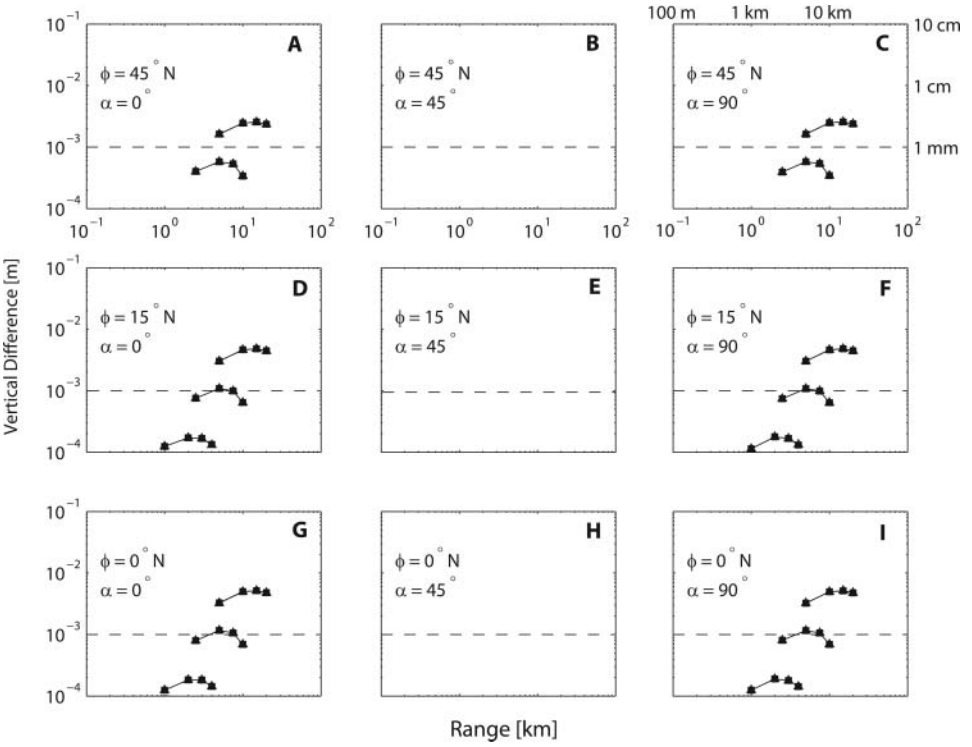

Figure 11. Vertical difference between Snell's Law planar form with earth flattening transformation applied using local mean radius, R_L (triangles), Gaussian mean radius, R_G (squares), and radius along the azimuth, R_α (circles) and the ellipsoid model. Note that the maximum vertical scale is reduced to 10 cm compared to 10 m in Figures 5 and 7. Separate plots show dependence on source latitude and ray azimuth. In all cases, choosing the radius along the azimuth, R_α, results in submillimeter agreement with the ellipsoidal earth ray-trace model.

and approximates the curvature in the direction from source to receiver. Both R_L and R_G reduce the maximum difference from 3 cm to 2 cm for the global means. For the special case of an azimuth of 45° (Figures 10 and 11 B, E, and H) all three radii, R_L, R_G, and R_α, equal the radius of the ellipsoid along the azimuth between source and receiver. However, choosing the radius along the azimuth, R_α, results in submillimeter agreement with the ellipsoidal-earth ray-trace model in all cases. This is a major finding of our analysis.

Finally, because thousands of acoustic rays are collected and traced as part of a seafloor geodetic experiment, reducing computation time is one goal of this study. Computation times were examined among the four approaches: ellipsoidal, spherical, planar, and straight-ray. To remove the characteristics of the specific platform used for the computations, we benchmarked the comparisons relative to the computation time for the ellipsoidal solution for each pair in the permutation set and compared these to the corresponding planar, spherical, and straight-ray computation times. The straight-ray approximation can be computed about 700 times faster than the ellipsoidal solution. The planar and spherical solutions can be computed about 32 times faster than the ellipsoidal solution.

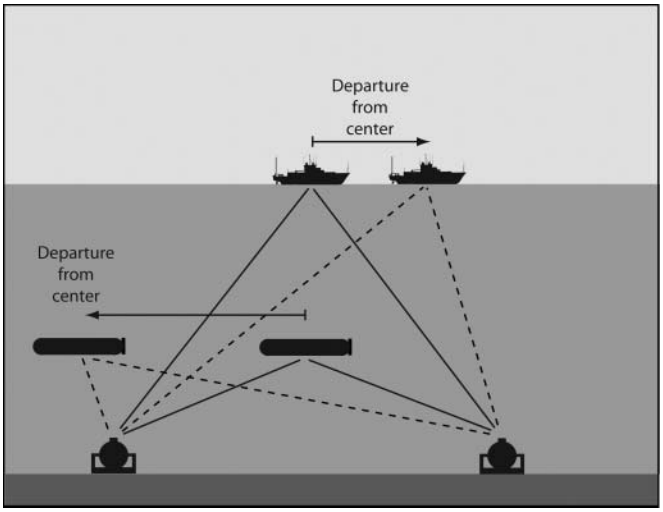

Figure 12. Departure of ship from center of seafloor array during GPS-acoustics operations and departure of underwater vehicle from center during near-bottom acoustic survey.

Impact of Approximation Errors on Indirect Path and GPS-Acoustic Positioning

Seafloor geodesy measures seabed displacement over time. Absolute errors common to all position measurements are of no affect. For example, with GPS-acoustics on a flat sea floor with the surface ship held precisely at the center of the array, all ray paths are equal length and equally affected by ray trace errors (Figure 12). Differencing these measurements in time to track displacement is free from ray trace errors regardless of the approximation. In practice, the ship cannot be held to a $\pm$1m location but drifts from approximately 5–10 m for a dynamically positioned vessel to 100 m or more for a manually steered vessel. As the lateral offset increases between the initial and subsequent ship locations, the magnitude of the approximation error changes and differencing the measurements no longer removes all the error. The difference or remaining error was calculated for all ray approximations as a function of lateral offset from the first to second vessel location for a GPS-acoustic scenario with water depth 2500 m and array separation of 5 km (Figure 13). For the straight-ray approximation, the nondifferenced error is 2 mm at 10 m lateral offset; for the planar approximation, the error is less than 1 mm up to approximately 200 m lateral offset. All earth-flattening transformed approximations have no remaining error above 1 mm for up to 10 km offset.

A similar analysis was conducted for a near bottom vehicle at 250 m altitude above the seafloor with an array separation of 2500 m and a water depth of 2500 m (Figure 12). Straight-ray approximation errors (Figure 14) remain below 1 mm for lateral separations up to 20 m while with Snell's Law with planar geometry approximation errors remain below the threshold up to 400 m. Again the earth-flattened approximations exhibit no error up to 10 km offset. Because near-bottom surveys require the vehicle to travel across the entire array to resolve seafloor positions, in most practical applications an earth-flattened approximation will be required.

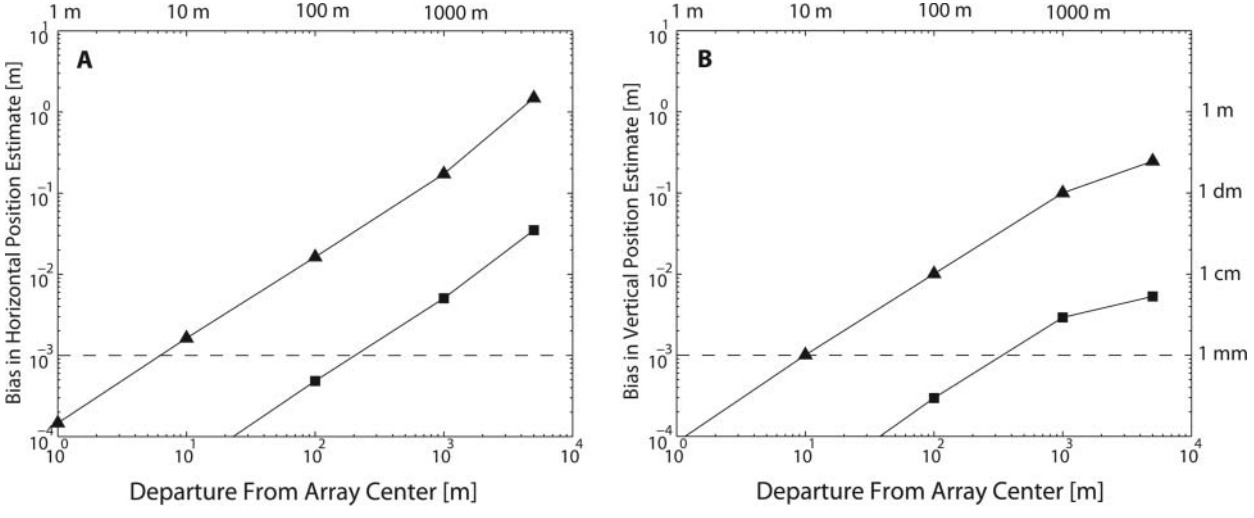

Figure 13. Bias in GPS-acoustic estimates of array position due to offset from center. Triangles are straight-ray and squares are Snell's Law with planar geometry. Circles are for Snell' Law with spherical geometry but are below the 0.1 mm minimum and not visible.

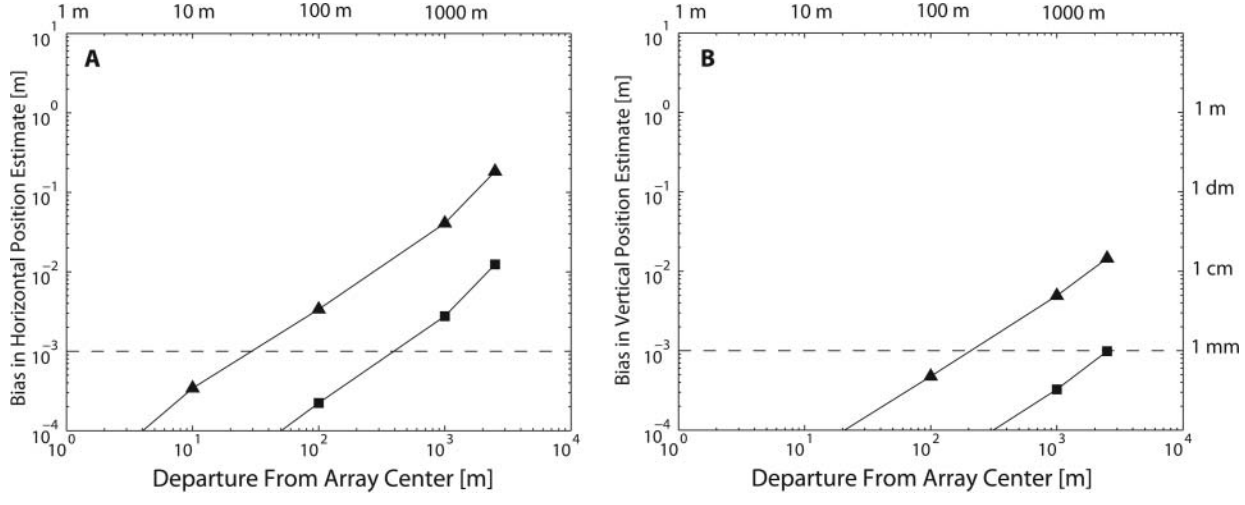

Figure 14. Bias in near-bottom survey estimates of transponder position due to offset from center. Triangles are straight-ray and squares are Snell's Law with planar geometry. Circles are for Snell' Law with spherical geometry but are below the 0.1 mm minimum and not visible.

Summary

Using an ellipsoidal form as the best representation of the earth, several alternative approximations were examined and compared: straight-ray with planar geometry, Snell's Law with planar geometry, and Snell's Law with spherical geometry via the earth-flattening transformation. Neglecting lateral variations in sound speed and geoid undulation, we find a useful approximation by combining a closed-form analytical solution of Snell's Law in planar geometry with an earth-flattening transformation that uses a mean ellipsoidal radius along the ray azimuth. This approximation is 32 times faster than integrating the full ellipsoidal equations. The approximation also agrees with the full ellipsoidal solution to within a millimeter up to distances of 20 km. This is achieved because the earth-flattening transformation approximates a sphere while using the mean ellipsoidal radius along the ray azimuth approximates the ellipsoid.

In applications of the GPS-acoustic technique, where the goal is to measure seafloor displacement of an array and errors common to all observations are of no effect, the straight-ray error remains below 1 mm if the ship can be held to within approximately 8 m of the same location throughout all surveys, which is reasonable for modern, dynamically positioned vessels. The computation time is reduced by a factor of 700. For Snell's Law with planar geometry, the lateral limit is 200 m, but applying the earth-flattening transformation extends the limit up to 10 km while maintaining a factor of 32 reduction in computation time over the ellipsoidal form. With near-bottom vehicle surveys that extend across the seafloor transponder array, Snell's Law with planar geometry and earth-flattening is required for arrays exceeding 400-m span. Finally, this paper examined distance errors resulting from approximating the ellipsoidal form of ray propagation equations. Timing errors, lateral and temporal sound speed variability, and lateral geoid undulation variability remain as additional error contributions.

Acknowledgements

This work was supported by BP America, Inc. and National Science Foundation grants OCE-0551765 and OCE-0850875 from the Marine Geology and Geophysics Program. We thank two anonymous reviewers for their thoughtful comments.

References

Biswas, N. N., and L. Knopoff. 1970. Exact earth-flattening calculation for love waves. *Bull. Seismo. Soc. Am.* 60:1123–1137.

Chadwell, C. D., J. A. Hildebrand, F. N. Spiess, J. L. Morton, W. R. Normark, and C. A. Reiss. 1999. No spreading across the southern Juan de Fuca Ridge axial cleft during 1994–1996. *Geophys. Res. Lett.* 26:2525–2528.

Georges, T. M., R. M. Jones, and T. P. Riley. 1986. Simulating ocean acoustic tomography measurements with Hamiltonian ray tracing. *IEEE J. Oceanic Eng.* OE-11;58–71.

Gagnon, K., C. D. Chadwell, and E. Norabuena. 2005. Measuring the onset of locking in the Peru-Chile trench with GPS and acoustic measurements. *Nature* 434:205–208.

Lemoine et al 1998. Development of the joint NASA GSFC and NIMA Geopotential Model EGM96. NASA/TP-1998–206861.

Munk, W. H. 1974. Sound channel in an exponentially stratified ocean, with application to SOFAR. *J. Acoust. Soc. Am.* 55:220–226.

Munk, W. H., W. C. O'Reilly, and J. L. Reid. 1988. Australia-Bermuda sound transmission experiment (1960) revisited. *J. Phys. Oceanogr.* 18:1876–1898.

Shockley, R. C., J. Northrop, P. G. Hansen, and C. Hartdegen. 1982. SOFAR propagation paths from Australia to Bermuda: Comparison of signal speed algorithms and experiments. *J. Acoust. Soc. Am.* 71:51–65.

Spiess, F. N., D. E. Boegeman, R. Zimmerman, C. D. Chadwell, and J. A. Hildebrand. 1997. MPL precision acoustic transponder. *SIO Reference* 97(3):1–15.

Spiess, F. N., C. D. Chadwell, J. A. Hildebrand, L. E. Young, G. H. Purcell, Jr., and H. Dragert. 1998. Precise GPS/acoustic positioning of seafloor reference points for tectonic studies. *Physics Earth Planet Int.* 108:101–112.

Sweeney, A. D., C. D. Chadwell, J. A. Hildebrand, and F. N. Spiess. 2005. Centimeter-level positioning of seafloor acoustic transponders from a deeply towed interrogator. *Marine Geodesy* 28:39–70.

Sweeney, A. D., C. D. Chadwell, and J. A. Hildebrand. 2006. Calibration of a seawater sound velocimeter. *IEEE J. Oceanic Eng.* 31(2):454–461.

Vincenty, T. 1975. Direct and inverse solutions of geodesics on the ellipsoid with application of nested equations. *Survey Rev.* 176:88–93.

Yan, J. 1999. Effects of earth curvature on two-dimensional ray tracing in underwater acoustics. *Appl. Acoustics* 57:163–177.